# Reduced Graphene Oxide-Based Flexible Pressure Sensor for Biomedical Applications

Alessandro Sanginario, *Member, IEEE*, Irene Buraioli, *Member, IEEE*, Marco Boscherini, *Member, IEEE*, Stefania Vitale, Conoci Sabrina, Daniele Botto, Dario Leone, Alberto Milan, Artur Ciesielski, Paolo Samorì, and Danilo Demarchi, *Senior Member, IEEE*

***Abstract*—Pressure sensing is a crucial technique for various biomedical applications, where it can provide valuable information about the health and function of different organs and systems. This article reports the development of a novel integrated pressure sensor based on modified reduced graphene oxide (rGO), a graphene-derivative material with enhanced piezoresistive properties. The sensor is fabricated on a flexible printed circuit board (PCB) substrate and conditioned by a smart current-based Wheatstone bridge circuit, which enables high sensitivity, wide detection range, fast response and recovery, and good stability under cyclic loading. The sensor achieves a measured sensitivity of 0.281 $kPa^{-1}$ (at 0.5 kPa load). A mechanical system is also designed to adapt the sensor to different anatomical sites and improve its elastic recovery. The sensor's functionality is initially demonstrated through its response to controlled mechanical stimulation, achieving a signal-to-noise ratio (SNR) of 25 dB. Subsequently, in a practical application, physiological signals from the carotid and femoral arteries of volunteers were acquired. The system effectively captured the pulse waveforms with high fidelity and accuracy (23.5-dB SNR) and measured the pulse transit time, an important parameter for estimating the pulse wave velocity (PWV) and arterial stiffness. The sensor is not limited to this specific application and can be easily extended to other domains where pressure sensing is required. In conclusion, it offers a low-cost, flexible, and user-friendly solution for noninvasive biomedical monitoring and diagnosis.**

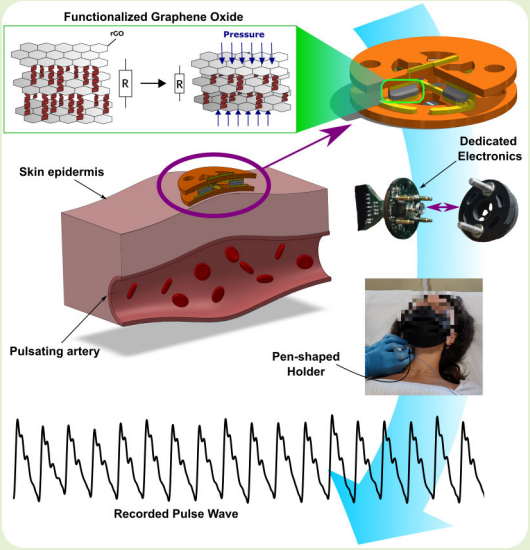


***Index Terms*— Biomedical pressure sensor, current-based Wheatstone bridge, flexible printed circuit board (PCB) sensor, reduced graphene oxide (rGO)-based pressure sensor.**

## I. Introduction

PRESSURE sensors are key tools for improving the quality of our planet as they offer vital functionalities enabling major steps forward in numerous upcoming technologies including robotics, biomedical devices for health monitoring and digital health care [1], environmental monitoring [2], wearables and foldable devices for human-machine interfaces, and electronic skin (E-skin) [3]. In the field of biomedical technologies, they hold great significance as noninvasive tools for monitoring several vital signs, contributing to an effective improvement of medical diagnosis. Within the cardiovascular field, they are employed not only for the heartbeat surveillance but also for the analysis of the arterial pulse wave to calculate the pulse wave velocity (PWV), considered a key parameter to assess arterial stiffness [4], [5], [6]. These sensors are also adept at monitoring breath rates through wearable devices, enabling a smart detection of respiratory dynamics [7], [8]. In addition, pressure and strain sensing systems have been widely considered for human motion and step monitoring for rehabilitation purposes [9], [10], [11].

Received 8 July 2024; revised 13 September 2024; accepted 22 September 2024. Date of publication 1 October 2024; date of current version 14 November 2024. The work of Paolo Samorì was supported in part by the European Union's Horizon Europe Research and Innovation Program through the project HYPERSONIC under Grant GA-101129613; and in part by ANR through the Interdisciplinary Thematic Institute SysChem via the IdEx Unistra within the program Investissement d'Avenir, the Foundation Jean-Marie Lehn, and the Institut Universitaire de France (IUF) under Grant ANR-10-IDEX-0002. The associate editor coordinating the review of this article and approving it for publication was Prof. Yu-Te Liao. *(Corresponding author: Alessandro Sanginario.)*

Please see the Acknowledgment section of this article for the author affiliations.

Digital Object Identifier 10.1109/JSEN.2024.3467995

© 2024 The Authors. This work is licensed under a Creative Commons Attribution-NonCommercial-NoDerivatives 4.0 License.
For more information, see https://creativecommons.org/licenses/by-nc-nd/4.0/

Ideally, an effective and reliable pressure sensor should meet several key requirements: high sensitivity is necessary to spot subtle pressure variations [12], [13], [14]; a wide detection range ensures versatility across multiple applications [15]; fast time response and recovery enable a correct acquisition of high-frequency pressure pulses and vibrations [16], [17], [18]; flexibility enhances the mechanical and electrical properties of the device, improves the sensitivity, and is fundamental for wearable applications [19]; and stability and robustness are important parameters as they determine the sensor's repeatability over time and lifespan [9], [20]. However, the development of sensors that combine all these advanced characteristics represents a major challenge in the field of device engineering. Depending on the application target, a tradeoff between these characteristics must be carefully considered to optimize the sensor's performance. With this purpose, various design strategies have been explored. Most of them encompass advanced material selection, surface functionalization, microstructure use, and optimization of geometric shapes and device architectures. Chen et al. [21] achieved a satisfying compromise among the main features previously listed. They developed a pressure sensor based on hierarchical conductive fabric, resulting in high sensitivity (15.78 $kPa^{-1}$), a wide-detection range (30 Pa–700 kPa), and excellent stability against deformation. Bai et al. [22] fabricated an iontronic flexible pressure sensor that demonstrated high sensitivity (49.1 $kPa^{-1}$) and linearity ($R2 > 0.995$) across a broad working range (up to 485 kPa). Moreover, such devices featured a fast response (<5 ms), enabling the detection of high-frequency pressure changes.

The fabrication of pressure sensors is strictly related to the transduction mechanism used to convert pressure into an electrical output, which depends on the material and the structure of the device [23], [24], [25]. Resistive pressure sensors utilize the piezoresistive effect, wherein the deformation of the sensing element (often a flexible diaphragm) leads to a resistivity variation, detectable with proper conditioning circuits. These types of sensors have been widely used for fundamental research and industrial applications due to their good characteristics in terms of sensitivity, sensing range, simplicity of manufacturing process, and signal acquisition. [26] Many different types of conductive carbon-based materials with an extended variety of designs have been employed to fabricate piezoresistive sensors [12], [27], [28], [29], [30], [31], [32], [33]. In piezocapacitive devices, the input pressure leads to a capacitance variation due to a change in the dielectric layer's dielectric constant in the distance between plates or their area [23], [34]. Capacitive sensors offer several advantages, such as stability, broad working range, and the possibility of proximity sensing [35], [36], [37]. However, these sensors' limitations lie in a slower response and recovery time concerning other technologies. Piezoelectric materials have also been employed to perform pressure measurements, thanks to their capacity to generate charges in response to the application of an external pressure [23], [38]. Their main characteristics are the capability to produce instantaneous voltage pulses, resulting in a very high-speed response, excellent sensitivity, and robustness. For this reason, they have been extensively utilized for collecting high-frequency pressure stimuli [39], [40]. However, they are unsuitable for static pressure acquisitions due to the pulsed nature of the output electrical signals.

Over the last couple of decades, graphene has stood out as a highly interesting material for designing piezoresistive pressure sensors, as it exhibits unique properties [41], [42], [43], [44], [45], [46]. In fact, its highest conductivity ($10e^6$ S/m at room temperature), resulting from a high electron mobility and saturation velocity, makes graphene suitable for electronic devices [47], [48]. On the other hand, its great elastic modulus $E$ (>1 TPa) and stretchability (>20%) confer to this material exceptional mechanical characteristics [49]. It is well-known that the sensitivity of a piezoresistive film is directly proportional to its thickness: for this reason, graphene, with its theoretical thickness of a single atom, is one of the most promising platforms for pressure sensors [50]. However, most research predominantly focuses on graphene derivatives, such as reduced graphene oxide (rGO). rGO, while exhibiting limited potential compared to pristine graphene in terms of electrical and mechanical properties due to its lower electrical conductivity and the presence of structural defects, offers greater scalability and ease of processability, making rGO-based pressure sensors more applicable for a wide range of uses [42], [51], [52], [53], [54], [55]. In a study by Tian et al. [56], a resistive pressure sensor consisting of laser-scribed graphene (LSG) films, derived from the reduction of graphene oxide (GO), was presented. The characterization of the LSG sensor demonstrated notable results in terms of sensitivity (up to 0.96 $kPa^{-1}$) across a moderate operational range (0–50 kPa).

In this work, we have exploited an already established sensory material based on chemically functionalized GO [57] and integrated this into a novel pressure sensor architecture. The novelty resides in the synergy between the integrated rGO-based transducing material, the shape of the sensor, and the widely available substrate technology.

The organization of this article is given in the following. Section II explores sensor design and fabrication characteristics, detailing considerations and characterizations crucial for developing the system's sensors. Moving on to Section III, the reading system is examined, focusing on the mechanisms and technologies responsible for interpreting signals from the sensors and converting raw data into meaningful information. Section IV focuses on firmware, delving into its crucial functions, algorithms, and role in ensuring proper operation and communication between system components. Section V introduces the graphical user interface (GUI), discussing the design and functionality of the interface that users interact with, encompassing aspects such as user experience and visual design. Section VI then explores the practical applications of the system, detailing its intended use cases and how it addresses a specific case scenario. Finally, in Section VII, the conclusions provide a comprehensive summary of key findings, contributions, and implications, touching on challenges, potential future research directions, and the overall significance of the project in a broader context.

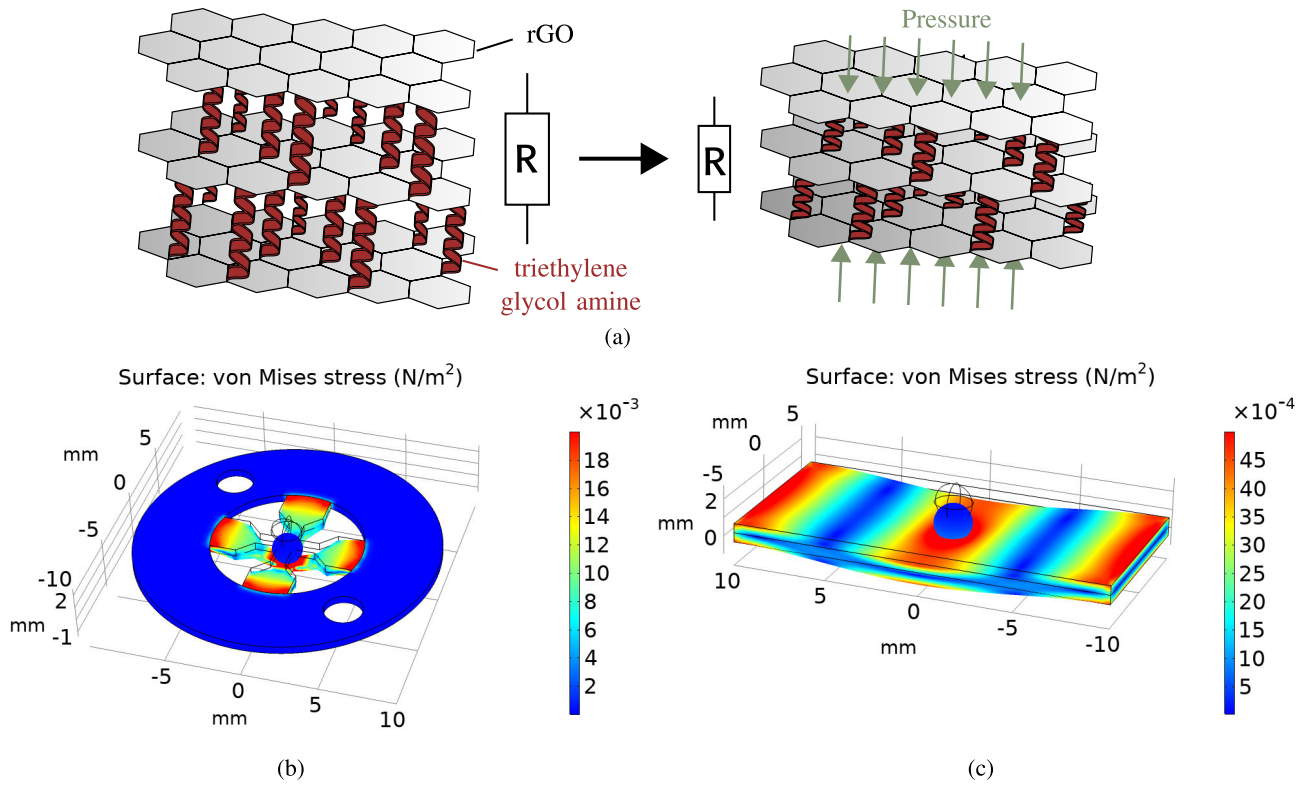


Fig. 1. (a) Triethylene glycol amine (*R***1**) acts as a microscopic spring, thanks to its mechanical flexibility. When compressed, the interlayer distance between the rGO sheets decreases, consequently reducing resistivity. Therefore, using a spring with a contour length of less than 2 nm imposes a spacing between lower than such a size; electronic crosstalk between adjacent graphene flakes in the stacks will be ruled by tunneling. This is key as its exponential relation between the measured current and the interflake distance endows a high sensitivity to tiny distance changes [57]. (b) and (c) COMSOL multiphysics[1] simulations to detect the maximum stress areas in the case of (b) cross-shaped and (c) rectangular sensor geometries.

## II. Sensor Design and Fabrication

The preparation of sensing material has been described in [57]. To help the reader, in Section II-A, we briefly recall its fabrication process. Sections II-A–II-D present sensor assembly and characterization from both technological and mechanical standpoints.

### A. rGO-R1 Fabrication Process

The pressure-sensing devices were prepared using a graphene-based material, rGO-R1, as a piezoresistive active component [57]. Such active material consists of rGO functionalized with the flexible molecular linker triethylene glycol amine. This was already shown to display excellent piezoresistive behavior compared to simple rGO, with a greatly enhanced response to the applied pressure in the 0.05–0.1-kPa range. rGO-R1 was used to assemble a flexible pressure-sensing device, which exhibited excellent properties in terms of sensitivity (as high as 0.82 $kPa^{-1}$), response time (24 ms), detection limit (7 Pa), durability (over 2000 cycles), and flexibility. First, graphene-based active material, rGO-R1, was prepared following a previously reported synthetic procedure consisting of two main steps: 1) the reaction of GO with triethylene glycol amine and 2) chemical reduction with $N_2H_4 \cdot H_2O$. Both reactions 1) and 2) were carried out by stirring overnight under reflux at 90 °C, under $N_2$ atmosphere, followed by purification through a sonication-centrifugation process (three cycles of 10 min at 2000 r/min). The resulting product, rGO-R1, was suspended in ethanol for a working dispersion of 0.5 mg/mL.

[1]Registered trademark.

### B. Working Principle

The proposed sensor comprises a thin layer of rGO-R1 deposited on a conductive surface. Utilizing a diaphragm as a flexible membrane, the sensor reacts to applied pressure by bending, consequently altering the resistance of the rGO-R1 layer [see Fig. 1(a)]. This change in resistance correlates directly with the amount of strain and is typically measured via a Wheatstone bridge. Like all piezoresistive sensors, the primary objective is to augment sensitivity by increasing the strain applied to the sensor. For this reason, considering the test case on which we validated the sensor, dedicated simulations were performed to assess the best position to deposit the piezoresistive material corresponding to the maximum stressed areas. Without going into details of the substrate, which will be described in Section II-D, we performed finite element (FE) simulations to locate the point of maximum deflection in the case of two different geometries: a rectangular one to directly compare with the substrate used in the previous work and a cross-shape one to increase the sensitivity.

### C. Simulations

The circular crown of the sensor was imposed to be mechanically fixed [blue colored in Fig. 1(b)], and a rounded-tip cylinder (represented only as a sphere in the simulation)

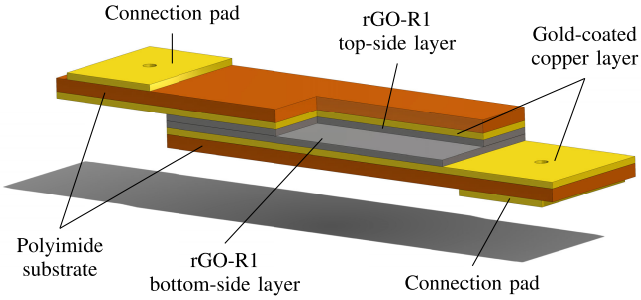


Fig. 2. Partial cross section of the rectangular-shaped sensor. The polyimide tape surrounding the sensor is not depicted. Image not to scale.

with a diameter of 2 mm was placed at the center of the cross. Finally, a load of 0.5 N was applied to the cylinder. Similarly, the rectangular sensor was mechanically fixed on its extremities [see Fig. 1(c)] with the same rounded cylinder tip simulating the load. Results, respectively, as shown in Fig. 1(b) and (c), indicate the maximum deflection to be located on the edge between the arms of the cross and the fixed circular crown and the center of the cross. In the case of the rectangular sensor, its stress distribution profile resembles that of the first shape, with notable stress concentrations at the edges and center. As expected, stress values of cross-shaped geometry are more than one order of magnitude higher. These results indicate that the cross-shaped sensor could obtain a better sensitivity with a more compact design; therefore, it could be the shape in which to invest our development efforts.

### D. Sensor Fabrication Process

The substrate used in [57] was a rectangular cut out of indium tin oxide (ITO)-coated poly(ethylene terephthalate) (PET). To overcome problems emerging with the asymmetric nature of the electrical contacts and the manual cutting procedure that could only output simple geometries, a very common yet technologically advanced substrate was chosen: polyimide printed circuit boards (PCBs). Polyimide PCBs present many advantages, such as high operating temperature, extremely high flexibility, and durability [58]. Moreover, it is possible to design any shape due to their standardized and consolidated manufacturing process. In addition, we chose to cover copper traces with gold using the electroless nickel immersion gold (ENIG) process as an additional service, as it protects the pads from oxidation and helps the adhesion of rGO-RI. Creating complex sensor shapes was then as simple as designing a standard PCB.

The preparation of pressure sensors onto rectangular (13 × 20 mm) and cross-shaped (20 mm diameter) flexible PCBs was carried out following a previously reported procedure [57], [59], with some modifications. Briefly, rGO-R1 active material was spray coated at 80 °C onto the gold-coated side of the PCBs substrates. Before the spray coating, a customized shadow mask was applied to create an rGO-free surface to place electrical contacts. For both rectangular- and cross-shaped geometries, 6 mL of rGO-R1 active material was spray-coated on the gold-coated side of the PCB substrates. After rGO-R1 deposition, the shadow mask was removed. Two of the obtained electrodes of analogous geometry were placed in a face-to-face configuration and fixed with polyimide (PI) tape (see Fig. 2). Regarding the cross-shaped geometry, instead of using PI tape to build the sensor, the two sides were placed face-to-face and kept in place using a custom-made 3D-printed holder. Electrical contacts were then obtained by soldering copper wires on areas not coated (green and red arrows in Fig. 3). In the rectangle-shaped sensor, the current enters from one contact pad, passes from one side to the other, and exits from the other connection pad. In the cross-shaped one, the current path is a bit more complex. Concerning Fig. 3, the current follows a single path, starting from the red arrow, and is forced to pass through four different rGO-R1 covered pads and, finally, exit from the green arrow. The four rGO-R1 pads are strategically placed in series, increasing the total sensor resistance to acquire a more easily readable resistance value (1–10 Ω).

### E. Characterization

*1) Deposition:* Sensor performances were investigated as a function of the active material content and the resulting coverage of the PCB surface. The deposition of rGO-R1 coatings on the PCB surface was assessed through SEM analysis, as reported in Fig. 4. As shown in [57, Fig. 2(a)–(i)], based on the amount of rGO-R1 dispersion spray-coated on the PCB, we can achieve different degrees of coverage of the PCB surface (namely, partial coverage, full coverage, and overload). Different surface coverage resulted in different performances in terms of durability and sensitivity.

*2) Piezoresistivity:* Fundamental characterization of the devices' performance was done on the rectangular sensors. Such performance was evaluated regarding pressure sensitivity and device durability upon application of cyclic stress. Such tests were carried out using a Mark-10 M7-025E digital force gauge mounted on a Mark-10 ESM-303E motorized test stand. The test setup had a round compression plate with a diameter of 1.15 cm. The sensitivity was assessed through static pressure tests, measuring the device's electrical resistivity when a static force was applied at 0.005–0.2 N (corresponding to a pressure range between 0.05 and 2 kPa). The resistivity was measured using a Keithley 2635B source meter. The durability of the devices was tested by cyclically applying a 0.5-kPa load and monitoring the change in electrical resistance over time using Labtracer. One-way analysis of variance (ANOVA) was used to evaluate statistical significance ($p < 0.05$). Error bars represent the standard error of the mean, extrapolated from separate experiments on at least five different samples.

With increasing the active material content and coverage of the PCB surface, the sensitivity of the PCB devices increases gradually [see Fig. 5(a) and Table I], going from 0.025 $kPa^{-1}$ when partial coverage is achieved to 0.281 $kPa^{-1}$ when full coverage is achieved. Further increase in the rGO-R1 content (overload) on the PCB surface results in a lower sensitivity of 0.137 $kPa^{-1}$. In all cases, the sensors also showed good linearity in the low-pressure range, as illustrated in Fig. 5(b).

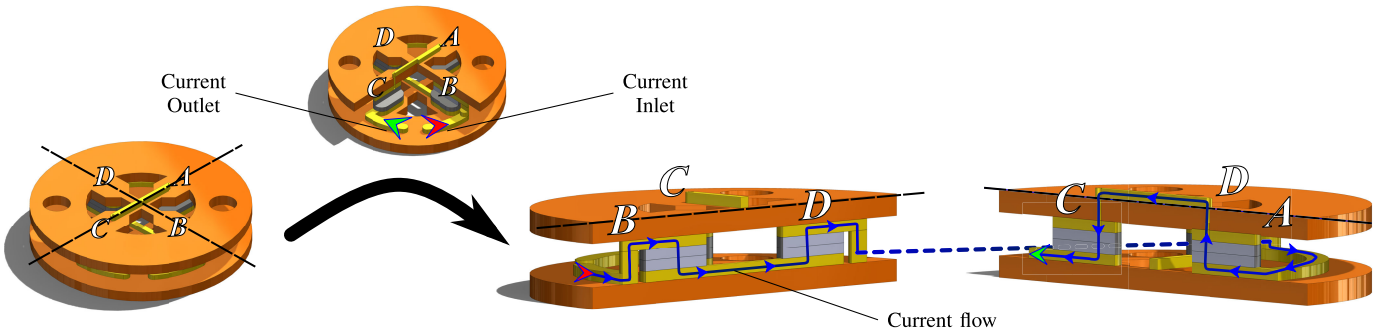


Fig. 3. Cross sections of rectangular sensor. The current flow starts from the red arrow, passes through four different rGO-R1 pads in series, and, finally, exits from the green arrow.

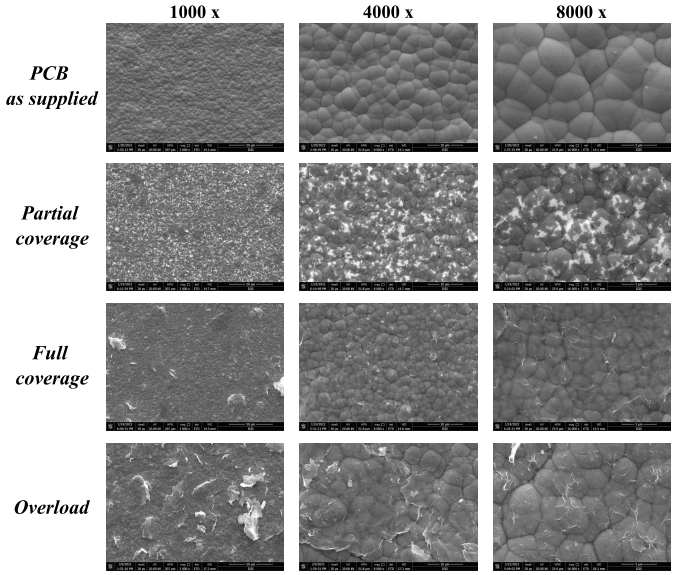


Fig. 4. SEM images for ITO-PET substrates before and after deposition of rGO-R1 in different proportions.

TABLE I
SENSITIVITY VALUES CALCULATED FOR DIFFERENT rGO-R1-BASED PRESSURE SENSORS

| Sample | Sensitivity ($kPa^{-1}$) | $R^2$ |
|---|---|---|
| PCB only | 0.013 | 0.93 |
| PCB + rGO-R1 (partial coverage) | 0.025 | 0.91 |
| PCB + rGO-R1 (full coverage) | 0.281 | 0.98 |
| PCB + rGO-R1 (overload) | 0.137 | 0.99 |

The PCB–rGO-R1 pressure sensors' robustness and stability were assessed through fatigue tests, carried out by applying a 0.5-kPa load in press-release cycles 1000× [see Fig. 5(c) and Table II]. A significant loss in device sensitivity (more than 60%) is observed in the case of partially covered PCB surfaces and for overloaded devices. In both cases, the change in resistivity for the same applied load is accompanied by a degradation of the dynamic response to the mechanical stress, as can be observed from the change in the shape of the stress curves over time.

Better stability is observed for the pressure sensors with fully covered PCB surface, with a good dynamic response to pressure load–unload even after 1000 cycles. Since the cross-shaped sensor needed its fixture to be kept in place, previously mentioned tests were executed only with the rectangular sensor. To properly mechanically characterize the cross-shaped sensor, another kind of test was carried out closer to the final application.

TABLE II
PRESSURE SENSITIVITY AT 0.5 kPa FOR PCB-rGO R1 DEVICES BEFORE AND AFTER FATIGUE TEST

| Sensor | R/R0 at 0.5 kPa | R/R0 after 1000 cycles | Sensitivity loss |
|---|---|---|---|
| PCB (no active material) | 0.0038 (± 0.0003) | 0.0038 (± 0.0002) | N.A. |
| PCB + rGO-R1 (partial coverage) | 0.0157 (± 0.0071) | 0.0059 (± 0.0011) | -62% |
| PCB + rGO-R1 (full coverage) | 0.0335 (± 0.0023) | 0.0250 (± 0.0031) | -25% |
| PCB + rGO-R1 (overload) | 0.0647 (± 0.0040) | 0.0250 (± 0.0039) | -61% |

*3) Mechanical:* Sensors were characterized mechanically to assess their performance in terms of the correlation between the displacement of the graphene-based diaphragm and the voltage output of the system. Tests on rectangular and circular-shaped sensors evaluated the behavior and differences between variants.

Fig. 6 shows the experimental setup whose main components are listed in the following.

1) *Vibration Test System:* The main equipment of the experimental setup is the TIRA TV 51120 vibration test system, which consists of a vibration exciter (shaker) and its amplifier to generate and modulate the oscillatory stimulus respectively. The amplifier was fed with a waveform generated with a VirtualBench from National Instruments.
2) *Shaker–Sensor Interface:* The moving coil of the shaker was coupled with the sensor through a slender rod, called a stinger, to transmit the oscillatory stimulus. One extremity of the stinger is clamped on the moving coil, while the other extremity pushes the sensor's membrane. The free extremity of the stinger ends with a 3D-printed tip to ensure a precise application of the oscillating motion to the sensing element. Various tips were designed, which allow optimal adaptation to different shapes of sensor variants.
3) *Sensor's Support:* Different 3D-printed housings were designed for the rectangular and circular sensors to

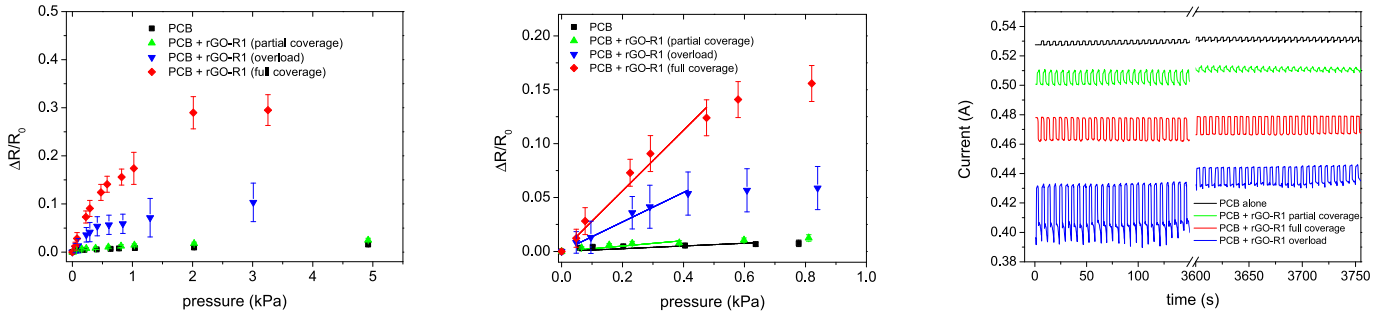


Fig. 5. (a) Relative resistance as a function of the applied pressure for different devices. (b) Sensitivity in the low-pressure range regime. (c) Fatigue tests under cycling application of 0.5-kPa load over time.

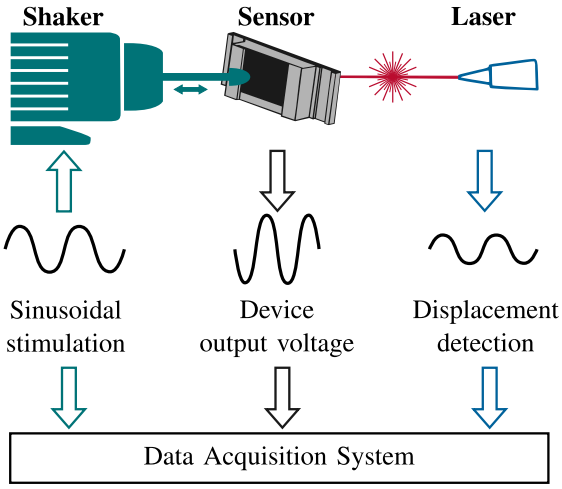


Fig. 6. Experimental setup for the mechanical characterization of the sensors. The shaker applies a sinusoidal vibration transmitted to the sensor's center through a stinger. A vibrometer (laser) detects displacements of the diaphragm. A data acquisition system collects the data. The experiment repeats for both the rectangular and the circular sensors.

ensure stability and proper positioning during the experiments. These housings were mounted on a metal stand, which, in turn, was attached to the working table with screws.

4) *Laser Vibrometer:* The displacement of the sensors was precisely measured with a laser Doppler vibrometer (LDV). Because the LDV is a noncontact measurement system, the membrane velocity was accurately measured without interfering with surface motion. The velocity was then converted to displacement by trapezoidal numerical integration.
5) *Data Acquisition System:* The velocity measured by the LVD, voltage, and current feeding the shaker were collected by an acquisition card, plotted online for immediate checking, and stored on the hard disk by in-house software. An experimental protocol was designed to recreate a simplified version of a pressure signal typical of the target application. For this purpose, the characteristics of the oscillatory stimulus were set up as shown in the following:
   a) sine wave stimulation;
   b) 1-Hz frequency (similar to the pulse signal range);
   c) low shaker voltage amplitudes to generate small displacements (of the order of hundreds of micrometers);
   d) various voltage amplitudes for different tests;
   e) application of a displacement offset to reproduce static pressure, which is always present during pulse acquisitions.

The mechanical characterization was carried out on both rectangular and cross-shaped sensors, setting sinusoidal stimuli of different amplitudes and acquiring the resulting voltage output from the device. The amplitude of the stimulation was progressively incremented until a plateau was reached, as shown in Fig. 7. While the rectangular sensor showed a steeper curve for lower displacements, the circular cross-shaped sensor proved better performance for higher ranges.

For each acquisition, the voltage output of the devices was compared with the displacement curve derived from the integration of the velocity data obtained from the vibrometer. The output signals exhibit a counterphase relationship with the sinusoidal displacement. This finding is consistent with the predicted behavior, indicating a resistance decrease as pressure increases.

The rectangular sensor produces quasi-sinusoidal voltage outputs for small displacements, consistent with the input displacement. However, slight distortions around the peaks are observed for larger displacements [see Fig. 7(a)]. To quantify this assumption, the signal-to-noise ratio (SNR) was calculated for different displacement amplitudes (75 and 182 $\mu$m). These values were chosen to have a range of approximately 100 $\mu$m backward from the start of the plateau. The SNR resulted in the following.

1) $\text{SNR}_{75\ \mu\text{m}} \approx 21$ dB.
2) $\text{SNR}_{182\ \mu\text{m}} \approx 20$ dB.

In contrast, the circular sensor consistently exhibits the expected behavior for any value of applied displacement amplitude, as shown in Fig. 7(b), for smaller and larger displacement amplitudes, respectively. The response of the circular sensor is significantly closer to the desired characteristics than the rectangular sensor. With the same logic as for the rectangular sensor, the signal corresponding to 195 and 300 $\mu$m was taken into account. It results in that higher displacements produce higher SNRs.

1) $\text{SNR}_{195\ \mu\text{m}} \approx 19$ dB.
2) $\text{SNR}_{300\ \mu\text{m}} \approx 25$ dB.

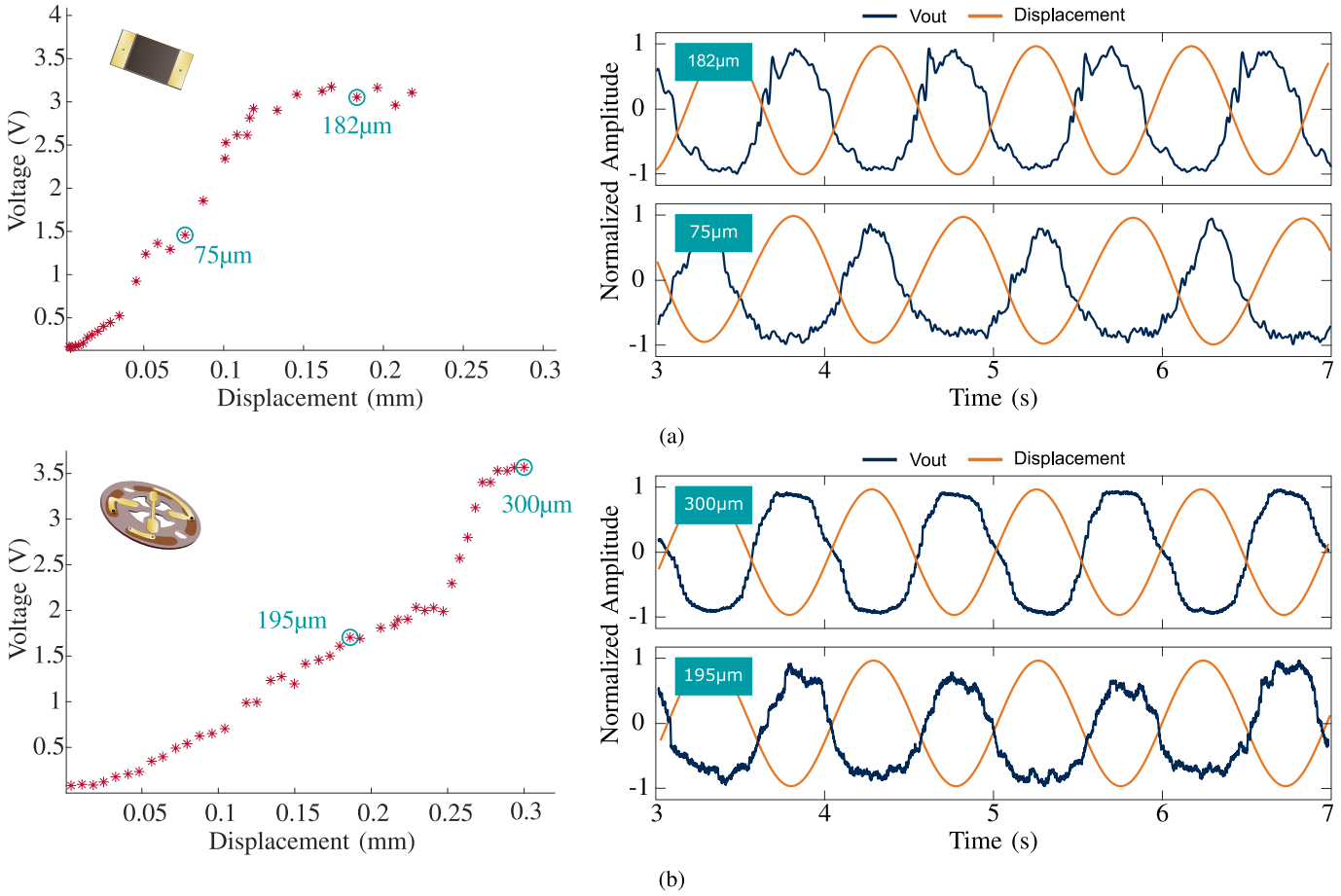


Fig. 7. Relationship between the output voltage of the device and the displacements (red) obtained during the mechanical characterization of (a) rectangular and (b) circular sensors. The tests were conducted by applying sinusoidal stimuli with progressive increments of amplitude until a plateau was reached. The plots on the right show the system's output voltage response (blue) compared to the sensor displacements (orange), both normalized in the figure. These graphs are displayed for two displacement amplitude values for each sensor (75 and 182 $\mu$m for the rectangular sensor, 195 and 300 $\mu$m for the circular one).

## III. Reading System

Dealing with small resistance variations of the order of tens of mΩ requires properly designing a sensitive conditioning circuit to convert tiny pressure inputs into readable voltage outputs. Moreover, piezoresistivity changes over time depending on environmental conditions, such as temperature and humidity or loss of sensitivity due to structural defects that can occur across the sensor's lifespan [60], [61], [62]. For this study, we have designed and developed a readout circuit whose core relies on a smart current-based Wheatstone bridge. Fig. 8 provides an overview of the proposed readout circuit.

The circuit first transforms the bridge output current, which is proportional to the applied pressure, into a raw voltage signal and then processes it using analog blocks to make it ready for reading. An STM32 microcontroller unit (MCU) converts the analog output into digital data using an analog-to-digital converter (ADC) and sends it externally to a PC via USB. As displayed in Fig. 8(a), the circuitry splits into three different PCBs. The circular PCB matches the sensor's dimensions and connects to its pads through the use of spring-loaded connectors [see Fig. 8(b)]; moreover, it contains the first stages of the conditioning circuit, including the Wheatstone bridge. The raw signal travels via wires to a second PCB (main board), which further processes it. The main board physically and electrically attaches to an SF2W pyboard D-series, which integrates the MCU responsible for managing the acquisition and control of the entire circuit.

Sections III-A and III-B present more detailed descriptions of the various stages of the circuitry.

### A. Current-Based Wheatstone Bridge

Fig. 8(c) shows an high-level representation of the readout schematic. For this study, a current-based Wheatstone bridge configuration, based on the circuit exploited in [63], was adapted to readout the resistance changes of the sensor. This configuration proved high accuracy (<0.001 mΩ) due to its capability of self-balancing. As widely recognized, the typical resistive Wheatstone bridge comprises four distinct resistors, which, when equal, maintain the bridge's balance. In our implementation (see Fig. 9), the sensor (indicated as $R_S$), placed in series with one of the four resistors ($R_1$), serves as the sole variable element in the configuration. Thus, a variation of the sensor's resistance induces imbalance to the Wheatstone bridge, with a consequent generation of nonnull output voltage ($V_{\text{OUT}}$) and currents ($I_A$ and $I_B$) whose difference ($I_{\text{OUT}}$) is

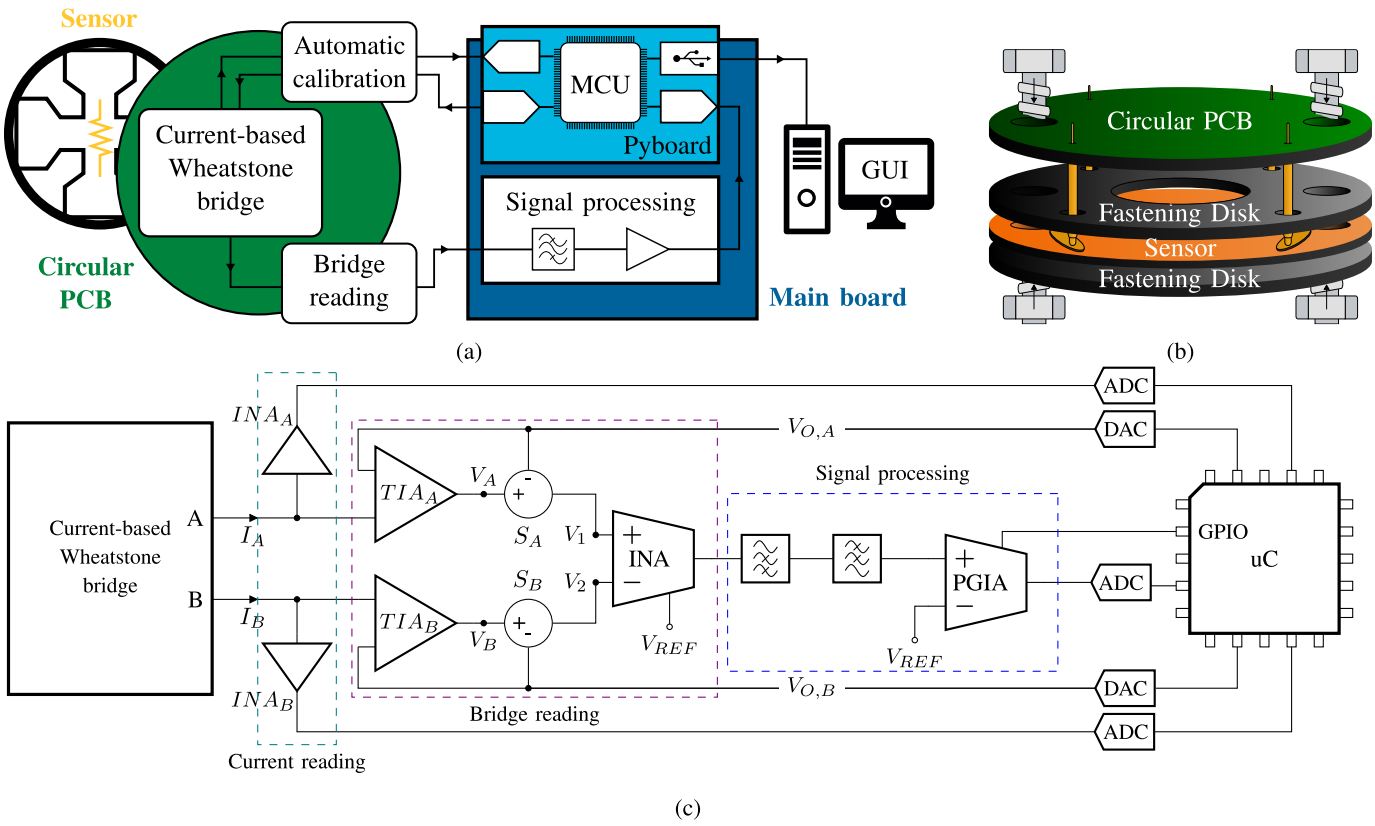


Fig. 8. (a) Readout circuit representation. The circuit is shared by three different PCBs: the circular PCB (green) directly connects to the pressure sensor, detects, and converts its resistivity variations into a voltage signal; the main board (dark blue) contains the signal processing stage and is fixed to a pyboard D-series (light blue). (b) Interface between the sensor and the circular PCB. Two 3D-printed disks keep the sensor steady. Four spring-loaded soldered to the circular PCB contact the sensor's conductive pads, performing the electrical connection. Two screws fasten the whole sensing system. (c) Block diagram of conditioning circuit. Dashed boxes surround different functional sections of the circuit.

proportional to the sensor's resistance variation. In a current-based approach, $I_{\text{OUT}}$ is the conditioned output signal, and it can be calculated as

$$\begin{aligned} &I_{\text{OUT}} \\ &= I_B - I_A \\ &= \frac{V_{CC}}{2} \frac{(R_1 + R_S)R_2(R_4 - R_3) - R_3R_4(R_2 - (R_1 + R_S))}{(R_1 + Rs)R_2R_3R_4}. \end{aligned} \tag{1}$$

If $R_0 = R_1 = R_2 = R_3 = R_4$, the previous formula can be simplified as

$$I_{\text{OUT}} = \frac{V_{CC}}{2} \frac{R_S}{R_0(R_0 + R_S)}. \tag{2}$$

The sensitivity of a conditioning circuit can be defined as the derivative of the output variable concerning the input one, as shown in (3). For the case under evaluation, if $R_0 \gg R_S$, it is possible to approximate the calculation as follows:

$$\begin{aligned} S_{C.Co} &= \frac{\partial I_{\text{OUT}}}{\partial R_S} \\ &= \frac{V_{CC}}{2} \frac{R_0^2 - R_S R_0}{(R_0(R_0 + R_S))^2} \\ &\approx \frac{V_{CC}}{2} \frac{1}{R_0^2}. \end{aligned} \tag{3}$$

*1) Bridge's Automatic Balancing System :* The self-balancing system was designed starting from two OAs, each connected to the corresponding Wheatstone bridge node ($A$ or $B$) through their inverting pins. Concerning Fig. 9, by applying a predefined offset voltage value ($V_{\text{OFF}}$) to the noninverting terminal, voltage levels are forced to the $A$ and $B$ output nodes of the bridge to find a balance to null the two output currents $I_A$ and $I_B$. This strategy ensures that even small changes in resistance within the bridge due to external factors such as temperature fluctuations or drifts over time do not significantly impact the output signal, leading to a more accurate measurement.

The determination of the offset values applied to the nodes $A$ and $B$ ($V_{O,A}$ and $V_{O,B}$, respectively) is automatically performed by the MCU, programmed to read the value of the output currents and generate the proper voltage offset to send to the OAs. To execute the current measurement, an instrumentation amplifier (INA) readouts and amplifies the voltage fall caused by the passage of the current through a resistor ($R_{\text{sense}}$), as shown in Fig. 9. The INA's output signal is transmitted to the MCU, where a dedicated "zeroing" algorithm takes charge.

*2) Bridge Reading:* With the completion of the calibration, the circuit is ready to perform the measurement, with $I_A$ and $I_B$, which predominantly reflect the sole pressure variations. The OAs employed for the bridge balancing play a dual role,

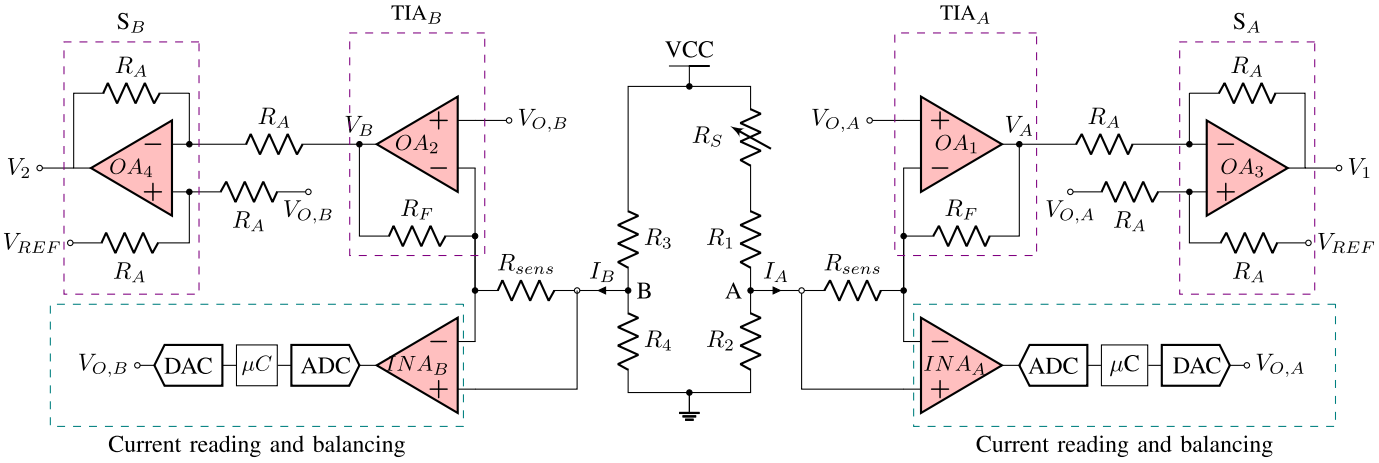


Fig. 9. Schematic of the adopted current-based Wheatstone bridge, with a voltage mode balancing configuration based on the use of two operational amplifiers (OAs) [63]. During the self-balancing phase, the current is measured by acquiring the voltage fall through $R_{\text{sense}}$. A microcontroller ($\mu$ C) calculates and sets one offset value for each side of the Wheatstone Bridge ($V_{O,A}$ and $V_{O,B}$) in order to minimize the current. During the acquisition phase, the output currents from the Wheatstone bridge ($I_A$ and $I_B$) are converted into voltages with TIAs (TIA$_A$ and TIA$_B$). $V_{O,A}$ and $V_{O,B}$ are, finally, removed from the signal by $S_A$ and $S_B$ to not affect the output signal from the balancing offset.

also serving as transimpedance amplifiers (TIAs) to convert the current signal into a voltage signal. The TIA output signal is determined by the value of the feedback resistor $R_F$

$$\begin{aligned} V_A &= -I_A R_F + V_{O,A} \\ V_B &= -I_B R_F + V_{O,B}. \end{aligned} \tag{4}$$

The previously applied offset is subsequently eliminated from the signal for both branches not to affect the measurement. This is accomplished by integrating a unity-gain inverting OA [represented as $S_A$ and $S_B$ in Fig. 8(c)] within the conditioning chain. This amplifier subtracts the $V_{\text{OFF}}$ value from the TIA output signal, nullifying the offset effect. Moreover, this stage shifts the output voltage to a predetermined reference voltage value, set at half of the voltage supply ($V_{CC}$), as shown in the following equation:

$$\begin{aligned} V_1 &= -V_A + V_{O,A} + V_{\text{REF}} \\ &= I_A R_F + \frac{V_{CC}}{2} \\ V_2 &= -V_B + V_{O,B} + V_{\text{REF}} \\ &= I_B R_F + \frac{V_{CC}}{2}. \end{aligned} \tag{5}$$

In addition, an INA is inserted to subtract and amplify the two resultant signals obtained from the left and right branches of the Wheatstone bridge

$$\begin{aligned} V_{\text{OUT}} &= G(V_2 - V_1) + \frac{V_{CC}}{2} \\ &= G R_F (I_B - I_A) + \frac{V_{CC}}{2} \\ &= G R_F I_{\text{OUT}} + \frac{V_{CC}}{2} \end{aligned} \tag{6}$$

where "$G$" is the gain of the INA, calculated as

$$G = 1 + \frac{100\ \text{k}\Omega}{R_g}. \tag{7}$$

From (6) and (2), it is possible to determine the value of $R_S$

$$R_S = \frac{2V_{\text{OUT}}R_0^2 - V_{CC}R_0^2}{V_{CC}R_0 - 2V_{\text{OUT}}R_0 + V_{CC}GR_F} \tag{8}$$

where "$V_{CC}$," "$R_0$," "$G$," and "$R_F$" are known and "$V_{\text{OUT}}$" is measured.

The circuit that has just been described is mounted on the circular PCB. The signal is sent to the main board via wires, where it will be further processed.

### B. Analog Signal Processing

The hardware processing stage commences with two third-order Sallen-key filters: high-pass filter (HPF) and low-pass filter (LPF). Specifically, each filter is created by the combination of first- and second-order filters, each characterized by its cutoff frequency. While the HPF attenuates the continuous and low-frequency components, the LPF reduces high-frequency noise. The characteristics of the signal under study guide the choice of the two cutoff frequencies. For this article's application focus, the bandwidth of interest spans from a fraction of hertz to a few tens of hertz. Consequently, cutoff frequencies of 0.1 and 20 Hz have been picked up.

The last analog stage of the conditioning circuit is a programmable-gain IA (PGIA) made of an INA and a multiplexer (MUX). The INA's gain is set by the value of an external resistor, as already shown in (7), which can be connected to specific amplifier terminals. In this system, eight different resistors have been used to set equal gains. By doing so, it is possible to adapt the signal dynamically to the ADCs, depending on the application and the magnitude of the pressure variation. This solution enhances the device's versatility, making it suitable for performing measurements with different working ranges. The resistors are connected to the INA through a MUX controlled by the MCU, which closes the switch corresponding to the selected gain.

The output analog signal is finally sent to the MCU board (pyboard D-series) and converted into digital data with an ADC.

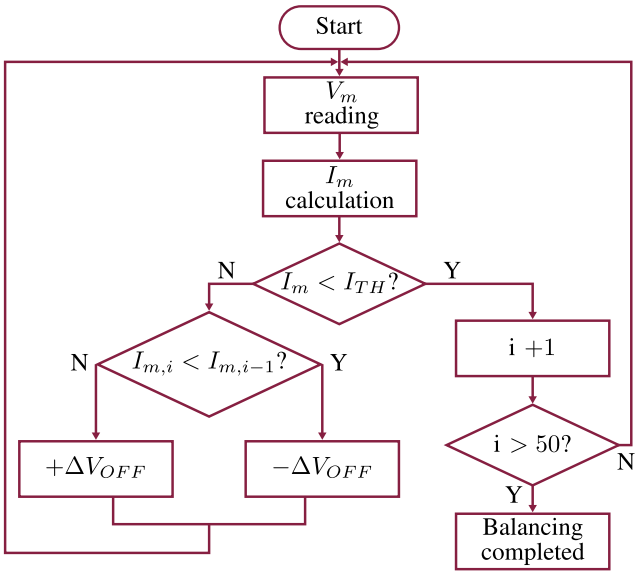


Fig. 10. Workflow of the automatic Wheatstone bridge balancing algorithm.

## IV. Firmware

We implemented the firmware in Micropython for the pyboard based on an STM32 MCU, which performs the different tasks in charge of the pressure-sensing system management. The script integrates different data acquisition and transmission functions, serial communication with the user, hardware component programming, and bridge balancing.

The firmware starts by configuring various components, such as ADCs, DACs, SPI, timers, and USB.

The first scheduled routine is the "current zeroing algorithm" for the automatic Wheatstone bridge balancing (see Fig. 10). The two offsets to apply to the noninverting inputs of the TIAs are both initialized as $V_{CC}/2$. To generate $V_{O,A}$ and $V_{O,B}$, the MCU programs two DACs integrated into the circular PCB via SPI communication. If $I_m$ exceeds $I_{\mathrm{TH}}$, the MCU adjusts $V_{O,A}$ in steps of $\Delta V_{\mathrm{OFF}}$ to decrease $I_m$ with respect to the previously measured value, and the algorithm starts over. When $I_m$ turns lower than $I_{\mathrm{TH}}$, a counter increments and a new iteration commences. If $(I_m)$ remains below $(I_{\mathrm{TH}})$ for 50 consecutive iterations (a reasonable compromise between time and accuracy), the right branch achieves balance, and the final $(V_{O,A})$ value is set. If not, the counter resets to zero, causing the process to recommence from the beginning. The whole algorithm repeats for the left branch of the Wheatstone bridge.

After the calibration is completed, the system is ready to start the acquisition of the signal. The data collection begins when the user sends the corresponding command to the MCU from the PC via USB. An ADC converts the analog signal into digital at a sampling frequency of 1 kHz to satisfy the bandwidth requirements imposed by the application of interest. The data are finally transmitted to the laptop via USB.

## V. Graphical User Interface

We also developed a GUI application with the Python programming language, intending to acquire the data and visualize them in real time (see Fig. 11). The software is primarily designed to diagnose biomedical signals but can be extended to other applications.

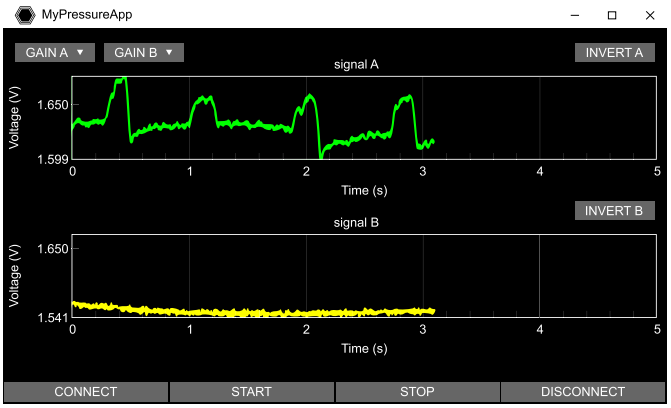


Fig. 11. Layout of the implemented GUI application.

The layout was defined using the Kivy framework, which enables the generation of screens and graphical widgets, such as control buttons or drop-down menus. The interaction with these widgets allows us to send commands to the MCU via USB and set different parameters. The screen splits into two distinguished graphs, allowing the simultaneous plotting of two signals, which is important for simultaneously monitoring the pulse wave signal from two different sites.

The communication with the serial port begins by clicking the "Connect" button, which connects to the device and starts the automatic calibration of the Wheatstone bridge. Once calibrated, a "Start" button enables digital signal acquisition. Samples are loaded into a buffer, saved to a text file, and displayed on a digital screen. Every 5 s, the input buffer updates with new data, autoscaling the $y$-axis for proper visualization. A drop-down menu allows the user to select the gain for the PGIA. Finally, the "Disconnect" button stops the real-time plotting, closes the serial communication, and turns off the GUI.

## VI. Application

This section presents a series of tests, conducted with the cross-shaped sensor, to showcase the sensor's effectiveness and translate the promising characterization results into practical applications. In this perspective, no comparisons with the state-of-the-art are performed since such preliminary tests have the unique purpose of demonstrating sensor potential in future biomedical device implementation. Pressure sensors have found applications across various domains, ranging from healthcare and biomedical research to industrial and consumer electronics. In this context, our primary focus revolves around the real-time screening of the arterial pulse, being part of research activities of our research group [64], [65], [66], [67], [68], [69], [70], [71]. Arterial pulse wave analysis can be performed to assess arterial stiffness and overall cardiovascular function by calculating the PWV.

### A. Mechanical System

In pursuit of creating a user-friendly device to perform the acquisition of the arterial pulse wave, we have designed

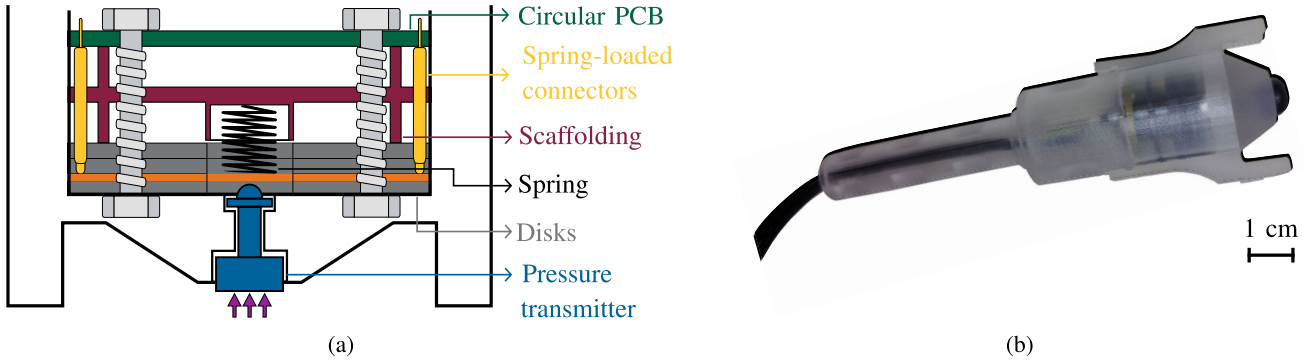


Fig. 12. (a) Illustration of a section of the pressure sensor holding system's tip: the 3D-printed pen (white) homes the sensing system, which is composed of the sensor (orange) kept steady by two plastic disks (dark gray), the circular PCB (spring-loaded connectors (yellow), a spring (black), screws, and the supporting scaffold (red). (b) Picture of the pen-shaped holder.

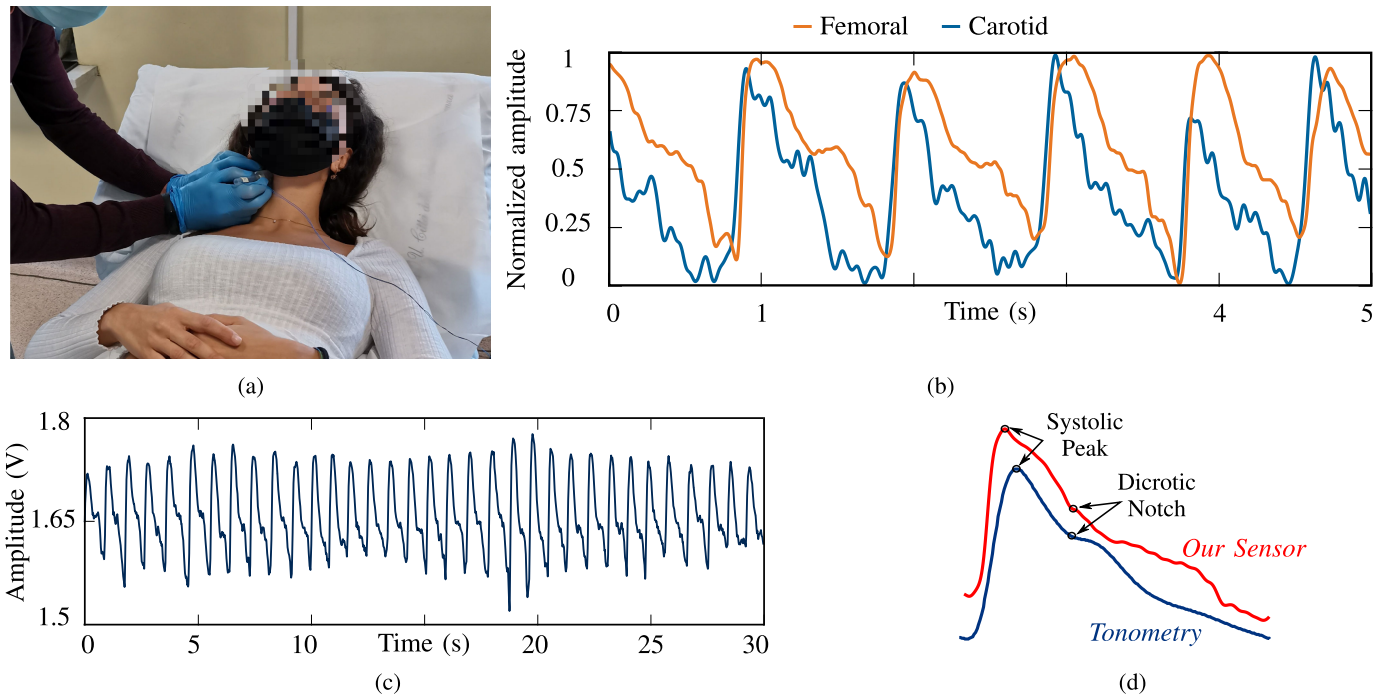


Fig. 13. (a) Pictures of a testing session during the acquisition of the pulse wave signal from the carotid artery. (b) Five seconds of simultaneous acquisition of carotid (blue) and femoral (orange) pulse wave signals using the developed device. (c) Pressure signal taken from the femoral artery of a volunteer during a 1-min acquisition. (d) Shape comparison between carotid pulses obtained by our sensor and reference technique.

a mechanical system tailored for this specific application (see Fig. 12). While initial testing with medical professionals indicates promising results, further studies are warranted to quantify the system's accuracy using established metrics. The sensor's case main structure is a pen-like shape holder intended for housing the device and guaranteeing comfortable handling by an operator. At one extremity, a fastening system allows for the interchangeability of different tips, constituting the interface between the pressure source and the sensor. In such a manner, the device offers adaptability to the anatomical characteristics of the artery and the surrounding tissues. The user can select one of the different available tips; each designed best to accommodate the anatomical features of the site under evaluation and easily assemble it on the holder. The pen's tip contains a pressure-transmitting system consisting of two integral components: a skin-side cylinder and a sensor-side tip. The dimensions of the skin-side cylinder are thought to match the diameter of the artery, ensuring precise and consistent contact. The sensor-side tip is positioned to apply pressure lengthwise at the center of the pressure sensor. The two components are affixed to the pen's tip and securely bonded using a resistant adhesive. To further enhance the usability and effectiveness of the device, the pen's tip presents two "wings" on the skin side. These wings serve as support to lay down the holder to the skin comfortably and create an outlet to reduce the static pressure value acting on the sensor. The sensor is inserted within the pen into a "pocket" to maintain stability during the measurements. The use of spring-loaded pins electrically interfaces the sensor and the circular board. To guarantee a reliable connection, we have incorporated two 3D-printed disks, positioning them on either side of the sensor. These disks are affixed to the PCB through

the use of four screws, thereby establishing a robust and enduring fastening. After being pressed, we observed a slow and incomplete elastic recovery, which, in turn, impacted the system's sensitivity during pulse wave acquisitions. To rectify this problem, a soft spring was integrated to improve the sensor's elastic properties without significantly affecting the measurement accuracy. This spring was positioned within a dedicated guide, engineered to create a contact only during the sensor's bending. This guide is part of a dual-role structure: keeping the spring steady in a perpendicular and centered way with respect to the sensor's cross, it works as a "scaffold" for the device, imposing a fixed distance between the two components. By adopting this solution, the forces applied to the sensor are balanced, including those from the spring-loaded connectors and the spring's compression forces.

The whole mechanical system is illustrated in Fig. 12(a). For the production of the components (holder, tips, disks, and scaffold), we employed a 3-D printer based on stereolithography technology.

### B. Application Examples

To roughly assess its functionality, one of the first trials involved the application of quick and controlled clicks with the index finger to the tip of the pen holder, housing the sensor. By doing so, we could evaluate its ability to register rapid pressure changes and promptly relay this data to the system for analysis.

Finally, we performed trials for acquiring physiological arterial pulse signals. To this end, a trained healthcare professional utilized our pressure-sensing system to collect pulse wave signals from the carotid and femoral arteries. We used the mechanical holder described earlier to ensure precision and comfort during measurements. This preliminary testing phase included a small and restricted group of volunteers. It aimed to validate, as a proof of concept, the device to prove its suitability for upcoming actual clinical trials.

Fig. 13(a) display a photograph of the experimental setup, with the operator using the pen holder to position the tips at the carotid site of interest.

To demonstrate the stability and reliability of the system, we conducted a session to gather data from a single site for a prolonged time. Fig. 13(c) presents a 30-s track of femoral pulse waves. The system could continuously record pulses with physiological shapes throughout the entire duration, with no performance degradation. To prove the quality of the acquired physiological signals, we calculated the SNR of more than 100 pulse waves and averaged the results, obtaining an SNR of 23.5 dB. This result is consistent with the SNR obtained during the mechanical characterization (see Section II-E.3).

Finally, we accomplished simultaneous acquisitions from both the carotid and femoral arteries, aiming to validate the system's intended application. We meticulously set up the experimental environment adopting the clinical conditions carried on at a hospital structure. The operator carefully positioned the two holders at the dedicated spots on the skin surface of the volunteers. During the trials, the professional received visual feedback via the developed GUI. In the postprocessing phase, we superimposed the two signals for comparison. An example of the results is presented in Fig. 13(b). As noticeable from the rising edges, the femoral pulse waves exhibited a slight time shift with respect to the carotid pulses, illustrating the expected delay in pressure transmission. This delay is known as pulse transit time (PTT), an important parameter for PWV estimation. These outcomes underscore the device's suitability for further clinical evaluations and applications, affirming its potential in medicine.

## VII. Conclusion

This article presented the design, fabrication, and characterization of a novel integrated rGO-based pressure sensor, suitable for various biomedical applications. The sensor is a thin layer of rGO-R1, a graphene derivative with enhanced piezoresistive properties, deposited on a flexible PCB substrate. The sensor exhibits high sensitivity, wide detection range, response time of 41 ms, which is perfectly adapted to pulse monitoring via biomedical pressure sensors, and good stability under cyclic loading. We have also developed a smart current-based Wheatstone bridge circuit to condition the sensor output and firmware to control the bridge balancing and data acquisition. Furthermore, we have designed a mechanical system to adapt the sensor to different anatomical sites and improve its elastic recovery. We have demonstrated the functionality of our sensor by acquiring physiological signals from the carotid and femoral arteries of volunteers, showing its ability to capture; according to an expert physician judge, the pulse waveforms are strongly comparable to the one recorded in clinical practice with Applanation tonometry techniques. This enables us to measure the pulse transit time, an important parameter for estimating the PWV and arterial stiffness. However, our sensor is not limited to this specific application and can be easily extended to other domains where pressure sensing is required. Our sensor offers a low-cost, flexible, and user-friendly solution for noninvasive biomedical monitoring and diagnosis.

## Acknowledgment

The authors would like to sincerely thank Professor Andrea De Marcellis for his support of the current-based Wheatstone bridge development.

Alessandro Sanginario, Irene Buraioli, Marco Boscherini, and Danilo Demarchi are with the Department of Electronics and Telecommunications, Politecnico di Torino, 10129 Turin, Italy (e-mail: alessandro.sanginario@polito.it; irene.buraioli@polito.it; marco.boscherini@polito.it; danilo.demarchi@polito.it).

Stefania Vitale, Artur Ciesielski, and Paolo Samorì are with ISIS, Université de Strasbourg & CNRS, 67000 Strasbourg, France (e-mail: svitale@unistra.fr; ciesielski@unistra.fr; samori@unistra.fr).

Conoci Sabrina is with the Department of Chemical, Biological, Pharmaceutical and Environmental Sciences, University of Messina, 98122 Messina, Italy (e-mail: sabrina.conoci@unime.it).

Daniele Botto is with the Department of Mechanical and Aerospace Engineering, Politecnico di Torino, 10129 Turin, Italy (e-mail: daniele.botto@polito.it).

Dario Leone and Alberto Milan are with the Candiolo Cancer Institute FPO-IRCCS, Division of Internal Medicine, Department of Medical Science, University of Turin, 10060 Turin, Italy (e-mail: dario.leone@ircc.it; alberto.milan@ircc.it).

## REFERENCES


[1] J. Hu, G. Dun, X. Geng, J. Chen, X. Wu, and T.-L. Ren, "Recent progress in flexible micro-pressure sensors for wearable health monitoring," *Nanosc. Adv.*, vol. 5, no. 12, pp. 3131–3145, 2023.

[2] Y. Duan, S. He, J. Wu, B. Su, and Y. Wang, "Recent progress in flexible pressure sensor arrays," *Nanomaterials*, vol. 12, no. 14, p. 2495, Jul. 2022.

[3] C. Xu et al., "Flexible pressure sensors in human–machine interface applications," *Small*, vol. 20, no. 15, Apr. 2024, Art. no. 2306655.

[4] A. Milan et al., "Current assessment of pulse wave velocity: Comprehensive review of validation studies," *J. Hypertension*, vol. 37, no. 8, pp. 1547–1557, Aug. 2019.

[5] C. B. Huang et al., "Highly sensitive strain sensors based on molecules–gold nanoparticles networks for high-resolution human pulse analysis," *Small*, vol. 17, no. 8, Feb. 2021, Art. no. 2007593.

[6] K. Meng et al., "Wearable pressure sensors for pulse wave monitoring," *Adv. Mater.*, vol. 34, no. 21, May 2022, Art. no. 2109357.

[7] K. Roy et al., "A self-powered wearable pressure sensor and pyroelectric breathing sensor based on GO interfaced PVDF nanofibers," *ACS Appl. Nano Mater.*, vol. 2, no. 4, pp. 2013–2025, Apr. 2019.

[8] J. Zhong et al., "Smart face mask based on an ultrathin pressure sensor for wireless monitoring of breath conditions," *Adv. Mater.*, vol. 34, no. 6, Feb. 2022, Art. no. 2107758.

[9] Y. Xiong et al., "A flexible, ultra-highly sensitive and stable capacitive pressure sensor with convex microarrays for motion and health monitoring," *Nano Energy*, vol. 70, Apr. 2020, Art. no. 104436.

[10] M. Bai, Y. Zhai, F. Liu, Y. Wang, and S. Luo, "Stretchable graphene thin film enabled yarn sensors with tunable piezoresistivity for human motion monitoring," *Sci. Rep.*, vol. 9, no. 1, p. 18644, Dec. 2019.

[11] L.-Q. Tao et al., "Graphene-paper pressure sensor for detecting human motions," *ACS Nano*, vol. 11, no. 9, pp. 8790–8795, Sep. 2017.

[12] X. Fu et al., "MXene/ZIF-67/PAN nanofiber film for ultra-sensitive pressure sensors," *ACS Appl. Mater. Interfaces*, vol. 14, no. 10, pp. 12367–12374, Mar. 2022.

[13] K. Ha et al., "Highly sensitive capacitive pressure sensors over a wide pressure range enabled by the hybrid responses of a highly porous nanocomposite," *Adv. Mater.*, vol. 33, no. 48, Sep. 2021, Art. no. 2103320.

[14] S. Song et al., "Bioinspired engineering of gradient and hierarchical architecture into pressure sensors toward high sensitivity within ultra-broad working range," *Nano Energy*, vol. 100, Sep. 2022, Art. no. 107513.

[15] G. Zhu et al., "3D printed skin-inspired flexible pressure sensor with gradient porous structure for tunable high sensitivity and wide linearity range," *Adv. Mater. Technol.*, vol. 7, no. 7, Dec. 2021, Art. no. 2101239.

[16] O. Legendre et al., "High-resolution micro-pirani pressure sensor with transient response processing and time-constant evaluation," *IEEE Sensors J.*, vol. 12, no. 10, pp. 3090–3097, Oct. 2012.

[17] J. Chen et al., "Ultrafast-response/recovery flexible piezoresistive sensors with DNA-like double helix yarns for epidermal pulse monitoring," *Adv. Mater.*, vol. 34, no. 2, Nov. 2021, Art. no. 2104313.

[18] J. Oh et al., "Highly uniform and low hysteresis piezoresistive pressure sensors based on chemical grafting of polypyrrole on elastomer template with uniform pore size," *Small*, vol. 15, no. 33, Aug. 2019, Art. no. 1901744.

[19] F. Xu et al., "Recent developments for flexible pressure sensors: A review," *Micromachines*, vol. 9, no. 11, p. 580, Nov. 2018.

[20] J. Lee, J. Kim, Y. Shin, and I. Jung, "Ultra-robust wide-range pressure sensor with fast response based on polyurethane foam doubly coated with conformal silicone rubber and CNT/TPU nanocomposites islands," *Compos. B, Eng.*, vol. 177, Nov. 2019, Art. no. 107364.

[21] T. Chen et al., "Highly sensitive and wide-detection range pressure sensor constructed on a hierarchical-structured conductive fabric as a human–machine interface," *Nanoscale*, vol. 12, no. 41, pp. 21271–21279, 2020.

[22] N. Bai et al., "Graded interlocks for iontronic pressure sensors with high sensitivity and high linearity over a broad range," *ACS Nano*, vol. 16, no. 3, pp. 4338–4347, Mar. 2022.

[23] Z. Shi et al., "Morphological engineering of sensing materials for flexible pressure sensors and artificial intelligence applications," *Nano-Micro Lett.*, vol. 14, no. 1, p. 141, Dec. 2022.

[24] A. Kumar, "Recent progress in the fabrication and applications of flexible capacitive and resistive pressure sensors," *Sens. Actuators A, Phys.*, vol. 344, Sep. 2022, Art. no. 113770.

[25] J. Huang, G. Xie, Q. Wei, Y. Su, X. Xu, and Y. Jiang, "Degradable MXene-doped polylactic acid textiles for wearable biomonitoring," *ACS Appl. Mater. Interfaces*, vol. 15, no. 4, pp. 5600–5607, Feb. 2023.

[26] H. Pan et al., "Biodegradable cotton fiber-based piezoresistive textiles for wearable biomonitoring," *Biosensors Bioelectron.*, vol. 222, Feb. 2023, Art. no. 114999.

[27] Q. Wu et al., "Triode-mimicking graphene pressure sensor with positive resistance variation for physiology and motion monitoring," *ACS Nano*, vol. 14, no. 8, pp. 10104–10114, Aug. 2020.

[28] Y. Ni et al., "Rational designed microstructure pressure sensors with highly sensitive and wide detection range performance," *J. Mater. Sci. Technol.*, vol. 130, pp. 184–192, Dec. 2022.

[29] S. Chen, Y. Song, and F. Xu, "Flexible and highly sensitive resistive pressure sensor based on carbonized crepe paper with corrugated structure," *ACS Appl. Mater. Interfaces*, vol. 10, no. 40, pp. 34646–34654, Oct. 2018.

[30] K. Singh, U. Valiyaneerilakkal, J. Akhtar, and S. Varghese, "Fabrication of poly (vinylidene fluoride-trifluoroethylene)—Zinc oxide based piezoelectric pressure sensor," *Sens. Actuators A, Phys.*, vol. 303, Mar. 2020, Art. no. 111677.

[31] L. Huang et al., "Three-dimensional light-weight piezoresistive sensors based on conductive polyurethane sponges coated with hybrid CNT/CB nanoparticles," *Appl. Surf. Sci.*, vol. 548, May 2021, Art. no. 149268.

[32] D. Kannichankandy et al., "Flexible piezo-resistive pressure sensor based on conducting PANI on paper substrate," *Synth. Met.*, vol. 273, Mar. 2021, Art. no. 116697.

[33] S. Pyo, J. Lee, W. Kim, E. Jo, and J. Kim, "Multi-layered, hierarchical fabric-based tactile sensors with high sensitivity and linearity in ultrawide pressure range," *Adv. Funct. Mater.*, vol. 29, no. 35, p. 1902484, Aug. 2019.

[34] R. Qin et al., "A new strategy for the fabrication of a flexible and highly sensitive capacitive pressure sensor," *Microsyst. Nanoeng.*, vol. 7, no. 1, p. 100, Nov. 2021.

[35] H. Guo et al., "Artificially innervated self-healing foams as synthetic piezo-impedance sensor skins," *Nature Commun.*, vol. 11, no. 1, p. 5747, Nov. 2020.

[36] R. B. Mishra, N. El-Atab, A. M. Hussain, and M. M. Hussain, "Recent progress on flexible capacitive pressure sensors: From design and materials to applications," *Adv. Mater. Technol.*, vol. 6, no. 4, Apr. 2021, Art. no. 2001023.

[37] J. Hwang, Y. Kim, H. Yang, and J. H. Oh, "Fabrication of hierarchically porous structured PDMS composites and their application as a flexible capacitive pressure sensor," *Compos. B, Eng.*, vol. 211, Apr. 2021, Art. no. 108607.

[38] Y. Su et al., "High-performance piezoelectric composites via $\beta$ phase programming," *Nature Commun.*, vol. 13, no. 1, p. 4867, 2022.

[39] D. Y. Park et al., "Self-powered real-time arterial pulse monitoring using ultrathin epidermal piezoelectric sensors," *Adv. Mater.*, vol. 29, no. 37, Oct. 2017.

[40] J. Yu et al., "Synergistic piezoelectricity enhanced $BaTiO_3$/polyacrylonitrile elastomer-based highly sensitive pressure sensor for intelligent sensing and posture recognition applications," *Nano Res.*, vol. 16, no. 4, pp. 5490–5502, Apr. 2023.

[41] K. S. Novoselov et al., "Electric field effect in atomically thin carbon films," *Science*, vol. 306, no. 5696, pp. 666–669, Oct. 2004.

[42] A. Ciesielski and P. Samorí, "Graphene via sonication assisted liquid-phase exfoliation," *Chem. Soc. Rev.*, vol. 43, no. 1, pp. 381–398, 2014.

[43] A. D. Smith et al., "Electromechanical piezoresistive sensing in suspended graphene membranes," *Nano Lett.*, vol. 13, no. 7, pp. 3237–3242, Jun. 2013.

[44] C. N. R. Rao, A. K. Sood, K. S. Subrahmanyam, and A. Govindaraj, "Graphene: The new two-dimensional nanomaterial," *Angew. Chem. Int. Ed.*, vol. 48, no. 42, pp. 7752–7777, Oct. 2009.

[45] A. D. Smith et al., "Pressure sensors based on suspended graphene membranes," *Solid-State Electron.*, vol. 88, pp. 89–94, Oct. 2013.

[46] V. Sorkin and Y. W. Zhang, "Graphene-based pressure nano-sensors," *J. Mol. Model.*, vol. 17, no. 11, pp. 2825–2830, Nov. 2011.

[47] K. I. Bolotin et al., "Ultrahigh electron mobility in suspended graphene," *Solid State Commun.*, vol. 146, nos. 9–10, pp. 351–355, Jun. 2008.

[48] V. E. Dorgan, M. H. Bae, and E. Pop, "Mobility and saturation velocity in graphene on $SiO_2$," *Appl. Phys. Lett.*, vol. 97, no. 8, Aug. 2010, Art. no. 082112.

[49] J.-U. Lee, D. Yoon, and H. Cheong, "Estimation of Young's modulus of graphene by Raman spectroscopy," *Nano Lett.*, vol. 12, no. 9, pp. 4444–4448, Sep. 2012.

[50] S.-C. Gong and C. Lee, "Analytical solutions of sensitivity for pressure microsensors," *IEEE Sensors J.*, vol. 1, no. 4, pp. 340–344, Dec. 2001.
[51] Y. Zhu et al., "Graphene and graphene oxide: Synthesis, properties, and applications," *Adv. Mater.*, vol. 22, no. 35, pp. 3906–3924, Sep. 2010.
[52] A. T. Smith, A. M. LaChance, S. Zeng, B. Liu, and L. Sun, "Synthesis, properties, and applications of graphene oxide/reduced graphene oxide and their nanocomposites," *Nano Mater. Sci.*, vol. 1, no. 1, pp. 31–47, Mar. 2019.
[53] H. Yao et al., "A flexible and highly pressure-sensitive graphene-polyurethane sponge based on fractured microstructure design," *Adv. Mater.*, vol. 25, no. 46, pp. 6692–6698, Sep. 2013.
[54] A. Tewari, S. Gandla, S. Bohm, C. R. McNeill, and D. Gupta, "Highly exfoliated MWNT-rGO ink-wrapped polyurethane foam for piezoresistive pressure sensor applications," *ACS Appl. Mater. Interfaces*, vol. 10, no. 6, pp. 5185–5195, Feb. 2018.
[55] Y. A. Samad, Y. Li, A. Schiffer, S. M. Alhassan, and K. Liao, "Graphene foam developed with a novel two-step technique for low and high strains and pressure-sensing applications," *Small*, vol. 11, no. 20, pp. 2380–2385, May 2015.
[56] H. Tian et al., "A graphene-based resistive pressure sensor with record-high sensitivity in a wide pressure range," *Sci. Rep.*, vol. 5, no. 1, p. 8603, Feb. 2015.
[57] C. Huang et al., "Molecule–graphene hybrid materials with tunable mechanoresponse: Highly sensitive pressure sensors for health monitoring," *Adv. Mater.*, vol. 31, no. 1, Jan. 2019, Art. no. 1804600.
[58] Z. Wu, J. He, H. Yang, and S. Yang, "Progress in aromatic polyimide films for electronic applications: Preparation, structure and properties," *Polymers*, vol. 14, no. 6, p. 1269, Mar. 2022.
[59] S. Vitale et al., "Tuning the piezoresistive behavior of graphene-polybenzoxazine nanocomposites: Toward high-performance materials for pressure sensing applications," *Chem. Mater.*, vol. 35, no. 17, pp. 6909–6919, Sep. 2023.
[60] A. A. Barlian, W. Park, J. R. Mallon Jr., A. J. Rastegar, and B. L. Pruitt, "Review: Semiconductor piezoresistance for microsystems," *Proc. IEEE*, vol. 97, no. 3, pp. 513–552, Mar. 2009.
[61] Z. Yao et al., "A high-temperature piezoresistive pressure sensor with an integrated signal-conditioning circuit," *Sensors*, vol. 16, no. 6, p. 913, Jun. 2016.
[62] Y. Liu, H. Wang, W. Zhao, H. Qin, and X. Fang, "Thermal-performance instability in piezoresistive sensors: Inducement and improvement," *Sensors*, vol. 16, no. 12, p. 1984, Nov. 2016.
[63] A. De Marcellis, C. Reig, and M.-D. Cubells-Beltran, "Current-based measurement technique for high sensitivity detection of resistive bridges with external balancing through control voltages," *IEEE Sensors J.*, vol. 17, no. 2, pp. 404–411, Jan. 2017.
[64] A. Sanginario et al., "Live demonstration: Wireless device for pulse wave velocity evaluation," in *Proc. IEEE Int. Symp. Circuits Syst. (ISCAS)*, May 2023, p. 1.
[65] A. Valerio et al., "Live demonstration: Wireless device for clinical pulse wave velocity evaluations," in *Proc. IEEE Biomed. Circuits Syst. Conf. (BioCAS)*, Union City, NJ, USA, Oct. 2022, p. 247.
[66] D. Leone et al., "Accuracy of a new instrument for noninvasive evaluation of pulse wave velocity: The arterial sTiffness faitHful tool assessment project," *J. Hypertension*, vol. 39, no. 11, pp. 2164–2172, 2021.
[67] I. Buraioli et al., "A new noninvasive system for clinical pulse wave velocity assessment: The athos device," *IEEE Trans. Biomed. Circuits Syst.*, vol. 15, no. 1, pp. 133–142, Feb. 2021.
[68] S. Conoci, F. Rundo, G. Fallica, D. Lena, I. Buraioli, and D. Demarchi, "Live demonstration of portable systems based on silicon sensors for the monitoring of physiological parameters of driver drowsiness and pulse wave velocity," in *Proc. IEEE Biomed. Circuits Syst. Conf. (BioCAS)*, Oct. 2018, pp. 1–3.
[69] I. Buraioli, D. Demarchi, A. Milan, F. Veglio, D. Leone, and F. Vallelonga, "Method and system for real-time measurement of the sphygmic wave velocity (pwv)," U.S. Patent App. 18 253 472, Dec. 28, 2023.
[70] A. Valerio et al., "A region-based cross-correlation approach for tonometric carotid–femoral pulse wave velocity assessment," *Biomed. Signal Process. Control*, vol. 93, Jul. 2024, Art. no. 106161.
[71] A. Valerio et al., "A new true wireless system for real-time pulse wave velocity assessment," *IEEE Sensors J.*, vol. 24, no. 15, pp. 24365–24376, Aug. 2024.

Open Access funding provided by 'Politecnico di Torino' within the CRUI CARE Agreement